Unprecedented enhancement of wear resistance for epoxy-resin graphene composites

Zhenyu Zhang,*[a] Yuefeng Du,[a] Chunhua Zhu,[b] Liangchao Guo,[a] Yao Lu,[c] Jinhong Yu,[d] Ivan P. Parkin,[e] Junhua Zhao,*[b] Dongming Guo[a]

[a]*Key Laboratory for Precision and Non-Traditional Machining Technology of Ministry of Education, Dalian University of Technology, Dalian 116024, China. E-mail: zzy@dlut.edu.cn*

[b]*Institute of Mechanics and Advanced Materials, School of Mechanical Engineering, Jiangnan University, Wuxi 214122, China. E-mail: junhua.zhao@163.com*

[c]*Department of Chemistry, School of Biological and Chemical Sciences, Queen Mary University of London, London E1 4NS, UK.*

[d]*Key Laboratory of Marine Materials and Related Technologies, Ningbo Institute of Materials Technology and Engineering, Chinese Academy of Sciences, Ningbo 315201, China.*

[e]*Materials Chemistry Research Centre, Department of Chemistry, University College London, 20 Gordon Street, London, WC1H 0AJ, UK.*

Abstract: Epoxy resins (ER) have extraordinary mechanical, electrical and chemical properties, and are widely used in aerospace, electronics and marine industries. Nonetheless, solidified ER have an intrinsic brittleness and low wear resistance. Up to now, the promotion of wear resistance of ER is limited to 30 times, through blending from one to four reinforcing materials. Therefore, it has been a challenge to enhance the wear resistance of ER to over 30 times. Additionally, the mechanisms to improve the tribological properties of polymer composites are elusive. In this study, novel ER/graphene composites (ECs) were developed, and the wear resistance of EC with 5 wt.% graphene (EC5) was shown to be 628 times that of pure ER at 10 N. To the best of our knowledge, the unprecedented enhancement of wear resistance for ER is the highest reported. The enhancement mechanisms of graphene reinforcement to ER were determined by molecular dynamics simulations. When the content of graphene reaches 5 wt.%, exfoliated graphene flakes adhere the most on the surface of a stainless-steel ball during sliding tests, reducing the wear most effectively. However, when the content of graphene is over 5 wt.%, graphene flakes accumulate inside the composites, and less exfoliated graphene flakes adhere to the surface of the ball during sliding, increasing the

wear. The developed binary ECs are light-weight, cost-effective and have minimal impact to the environment. This composite has many potential applications for high performance components used in aerospace, electronics and marine industries.

Keywords: Epoxy resin; graphene; composite; wear rate; wear mechanism

Introduction

Epoxy resin (ER) was firstly discovered in 1909,[1] and it has high adhesion strength, good heat resistance, excellent solvent, heat and chemical resistance, and high electrical resistance.[1-9] ER has good processing ability and low cost for preparation, and is one of the most widely used conventional thermosetting plastics.[3] It is broadly employed for three-dimensional (3D) printing,[10-13] semiconductor photocatalysts,[14] coatings,[15] nanomaterials,[16] foams,[17] metamaterials,[18] magnets,[19] and Li/K ion batteries.[20] ER is a sustainable resource, which is fabricated from renewable plants, such as soybeans, sunflower, castor oil plant and palm trees.[21] It is a substitute for petrochemical-derived polymers. Owing to the superior mechanical, electrical, and chemical properties and the fact that it can come from a renewable source, ER is widely applied in coating, adhesive, aerospace, electronics, biomedical and marine industries.[1-3] Nevertheless, solidified ER is brittle in nature, resulting in low fracture toughness and wear resistance.[2,15] In addition, stress is formed during curing in ER induced by a high crosslinking density.[2] For a brittle material, fracture strength is considered at the order of E/10, where E is the Young's modulus.[18] Due to the high crosslinking density and stress, the Young's modulus, yield stress, and fracture strength of ER are 2.6 GPa, 62.1 MPa and 65.5 MPa, respectively.[15] Low wear resistance of ER is not qualified for the use in high performance devices. As a result, it is essential to enhance the wear resistance of ER by reinforcements, to satisfy the stringent requirements of high performance moving mechanical components.

ER has a low wear resistance, which is fatal for moving mechanical components used for high performance devices. Therefore, the improvement on wear resistance of ER has attracted much attention.[22-25] Normally, single component reinforcement is used to reinforce the wear resistance of ER. For instance, waste tire rubber (WTR), carbon (C) nanotubes (CNTs), silica (SiO_2), C nanofibers (CNFs), silicon nitride (Si_3N_4), nano clay banana fiber, and natural sponge have been

employed to promote ER, and the wear resistance was increased 4.3, 5.5, 1.25, 5, 4.2, 2.9, and 1.8 times that of pure ER, respectively.[22] A fluoroepoxy oligomer was filled in ER, and the wear resistance enhanced by 10 times that of pristine ER.[23] Graphene exhibits unique and exceptional mechanical, thermal, electronic and chemical properties, becoming the most studied two-dimensional (2D) material.[26-32] It has an in-plane Young's modulus of 1 TPa, while the interlayer Young's modulus perpendicular to the plane is only 36 GPa.[33-35] The tremendous discrepancy between in-plane and off-plane modulus makes graphene potentially possess the leadership in the field of wear resistance.[36] Superlubricity has been realized by graphene at a nanoscale, microscale and macroscale.[37-40] Nonetheless, the wear resistance was enhanced by 1.4, 2, 7.6, 12.6 and 12.8 times through adding graphene nanoplatelets (GNPs),[22] graphene oxide (GO),[22] graphene,[41] functionalized GO[42] and amino-treated graphene (rGO)[43], respectively. To further intensify the wear resistance, binary reinforcements were blended in ER. For example, glass fiber (GF)-wall tile, hexagonal boron nitride (HBN)-cubic BN (CBN), CNF-molybdenum disulphide (MoS_2), CNFs-polyimide (PI), GO-polytetrafluoroethylene (PTFE), and CNTs-zinc sulfide (ZnS) were applied in ER, and the wear resistance heightened by 6.1, 8, 7.7, 6, 1.43, and 18 times, respectively.[22,44] With the growth of science and technology, ternary and quaternary hybrids were employed to intensify the wear resistance of ER. Silicon carbide (SiC)-MoS_2-graphite (Gr), and CNTs-short glass fiber (SGF)-short C fiber (SCF)-SiO_2 were used to reinforce ER, and the wear resistance was enhanced by 4 and 9 times, respectively.[22,45] Due to the remarkable properties of graphene, recently the wear resistance of ER has been shown to be promoted 30 times by ternary CNTs-GO-MoS_2[25] hybrids. However, when the hybrids are more than two kinds of materials, the fabrication processes are complicated and difficult to control. Thus, it is vital to reducing the hybrids to one or two kinds of materials. Furthermore, the present reinforcements in ER induce four disadvantages, consisting of environmental pollution, increases of volume and weight, limited enhancement ability and low contact area between ER and reinforcements. It is a great challenge to increase the wear resistance of ER over 30 times, according to the present state-of-the-art technologies.

Molecular dynamics (MD) simulations are effective and indispensable to explore the tribological mechanisms of graphene sheet (GS)/polymer composites. Nevertheless, during the past two decades, MD simulations were dedicated to investigating the tribological properties of pure

polymer materials, including polymer brushes, lubrications and dry friction.[46] Until now, very few works focused on GS/polymer composites. Fundamental mechanisms on improvement of tribological properties for GS/polymer composites are elusive. It is necessary to note that the exploration for tribological mechanisms of GS/polymer composites is still at an early stage. For instance, a single GS or CNT is embedded in a composite matrix to investigate the mechanical properties, such as hardness, shear modulus, Young's modulus, and tribological performance through pull-out processes for friction measurements.[46-51] Moreover, at present, the simulation scale of MD is very small. For example, an MD model of CNT/styrene-butadiene rubber (SBR) consists of only 3902 atoms for simulating frictional processes.[46] Current studies only pay attention to the physical interactions during frictional processes for GS/polymer or CNT/polymer composites.[46] MD simulations on tribological properties for crosslinking between dispersed graphene and polymer matrix have not been reported.

In this study, seven kinds of binary ECs were fabricated, and their wear resistance was over 30 times that of pristine ER. Enhancement mechanisms of ECs were elucidated by MD simulations, through crosslinking between curing agent and polymer, and blending dispersed graphene randomly in ER.

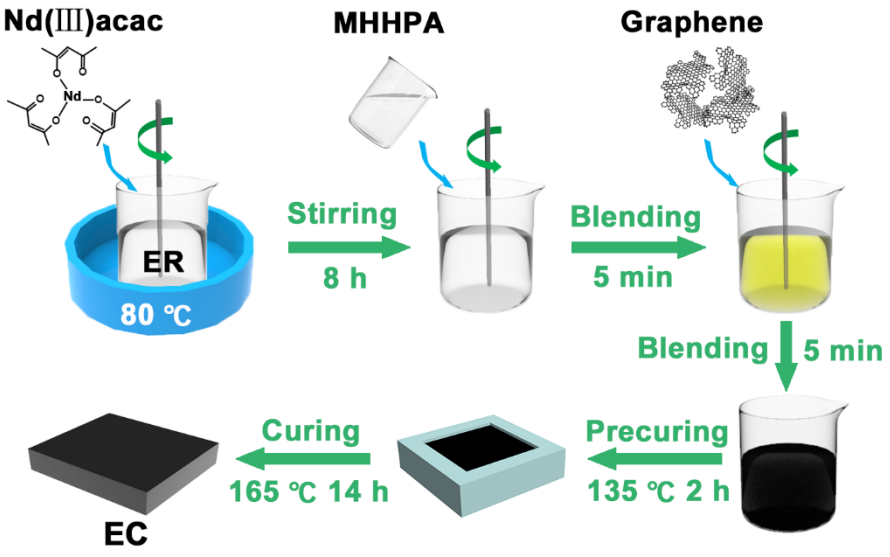

Figure 1 Schematic diagram of preparation processes for ECs.

Results and discussion

Figure 1 shows the schematic diagram of preparation processes for ECs. Firstly,

neodymium(III) acetylacetonate trihydrate ($Nd(acac)_3.3H_2O$) was poured in ER, then stirred at 80 ℃ for 8 h. Subsequently, methylhexahydrophthalic anhydride (MHHPA) was added and stirred for 5 min, incorporating graphene, blending for 5 min, pro-curing for 2 h at 135 ℃, curing for 14 h at 165 ℃, and finally generating ECs. To distribute the graphene in ECs uniformly, the liquid ECs were magnetically stirred for 5 min. After magnetic stirring, the graphene was uniformly distributed in ECs. With this method, seven kinds of graphene/ER composites were prepared. For comparison, pure ER was also produced. Figure S1 depicts the photographs of prepared pure ER and ECs with different contents of graphene. ECs with 1, 2, 3, 4, 5, 6, 7 wt.% graphene are designated as EC1, EC2, EC3, EC4, EC5, EC6, and EC7, respectively. Pure ER is transparent, as shown in Fig. S1(a). After blending with the graphene, ECs become non-transparent and black (Figs. S1(b)-S1(g)). With increasing the content of graphene, ECs get blacker and blacker.

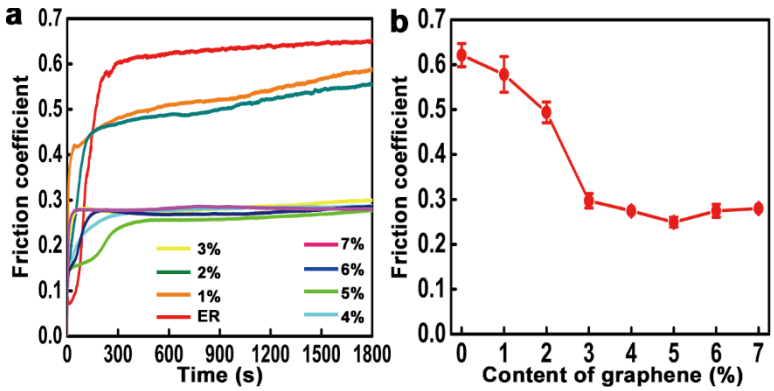

Figure 2 Friction coefficient of pure ER and ECs at 10 N as a function of (a) time and (b) content of graphene.

Figure 2 illustrates the friction coefficient of ER and ECs at 10 N as a function of time and content of graphene. Friction coefficient, μ is defined,[39]

$$\mu = \frac{F_l}{F_n} \qquad (1),$$

where, F_l and F_n are the lateral and normal forces, respectively. The friction coefficient of ECs is stable between 400 to 1800 s at a normal load of 10 N (Fig. 2(a)). Dynamic sliding process at 10 N for EC5 is displayed in Movie S1. With blended graphene, all the friction coefficients of ECs are lower than that of pure ER (Figs. 2(a) and 2(b)). Friction coefficient of ER is 0.62, which is in good agreement with those of previous reports.[52,53] The EC5 has the lowest friction coefficient of 0.25

(Fig. 2(b)), which reduces 60% compared to that of pure ER. With increasing graphene content, the friction coefficient of ECs decreases initially, and then increases.

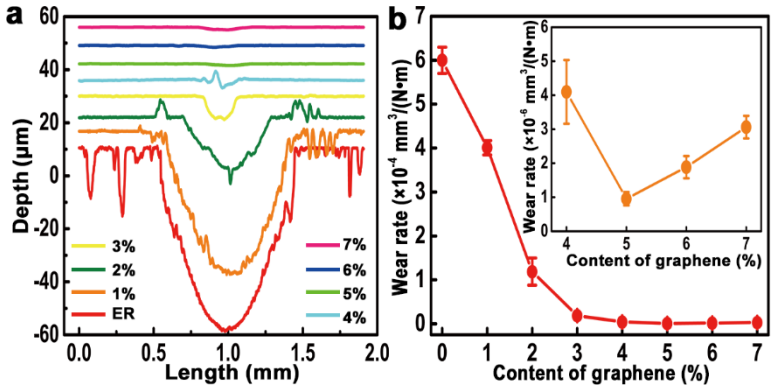

Figure 3 (a) Depth profile of wear tracks, and (b) wear rate at 10 N as a function of content of graphene for pure ER and ECs. Inset in (b) showing the corresponding enlarged part of wear rate as a function of content of graphene from 4 to 7 wt .%.

Figure 3 shows the depth profile of wear tracks and wear rate at 10 N for pure ER and ECs. With blended graphene, all the worn areas of the depth profiles of the wear tracks for ECs are lower than that of pure ER (Fig. 3(a)), resulting in a lower wear rate (Fig. 3(b)). Wear rate, W_r is calculated,[54]

$$W_r = \frac{AL}{F_n S} \qquad (2),$$

where, A and L are the area of depth profile and length of wear tracks respectively, and S is the sliding distance. EC5 has the smallest area of depth profile (Fig. 3(a)) and the lowest wear rate (Fig. 3(b)), which is consistent with the lowest friction coefficient shown in Fig. 2. With mixing graphene, the wear rate of ECs decreases initially, and then increases, which is consent with the variation of friction coefficient in Fig. 2. Wear rate of pure ER at 10 N is 6×10^{-4} $m^3/(N\cdot m)$ (Fig. 3(b)), which is in good agreement with those previously reported.[23,25,52] The EC5 has a wear rate of 9.55×10^{-7} $m^3/(N\cdot m)$, demonstrating an unprecedented enhancement of wear resistance by 628 times that of pure ER. In Fig. 3(b), the wear resistance of EC1, EC2, EC3, EC4, EC5, EC6, and EC7 are 1.5, 5, 32, 146, 628, 319, and 196 times that of pure ER, respectively. The wear resistance for EC4, EC5, EC6 and EC7 was enhanced by two orders magnitude higher than that of pure ER. Usually, the enhancement of wear resistance is limited to 30 times induced by a ternary hybrid of CNTs-GO-

MoS_2 in ER.[22] To the best of our knowledge, our work demonstrates the highest wear resistance by the EC5, in comparison with those reported in previous literature.[22]

Friction coefficient of ER at 8 N and 6 N is 0.56 and 0.61, respectively, as illustrated in Figs. S2 and S3. This is consistent with 0.62 of ER at 10 N (Fig. 2). For blending graphene from 4 to 7 wt.% in ER, the friction coefficient of ECs at 8 N and 6 N stabilizes at approximately 0.28, reaching the lowest value and reducing by 50% and 54% that of ER (Figs. S2 and S3). Dynamic sliding processes at 8 N and 6 N for EC5 are displayed in Movies S2 and S3, respectively. Wear rates of ER at 8 N (Fig. S4) and 6 N (Fig. S5) are 8.52×10^{-5} and 9.8×10^{-5} $m^3/(N\cdot m)$, correspondingly, which is about 1/7 and 1/6 that of ER at 10 N. Decreasing load from 10 N to 8 N or 6 N, the wear rates of ER obviously decrease. Variation between friction coefficient and wear rate is consistent for both 8 N (Figs. S2 and S4) and 6 N (Figs. S3 and S5). For 8 N, wear resistance of EC1, EC2, EC3, EC4, EC5, EC6 and EC7 is 0.9, 1, 1, 51, 87, 43, and 35 times that of pure ER, respectively (Fig. S4), corresponding to 1, 1, 1, 57, 86, 50, and 40 times that of the latter at 6 N (Fig. S5). For both 8 N and 6 N, the lowest wear rates are obtained by the EC5. Furthermore, the wear resistance of EC4, EC5, EC6 and EC7 at 8 N and 6 N were enhanced over 35 times that of pure ER.

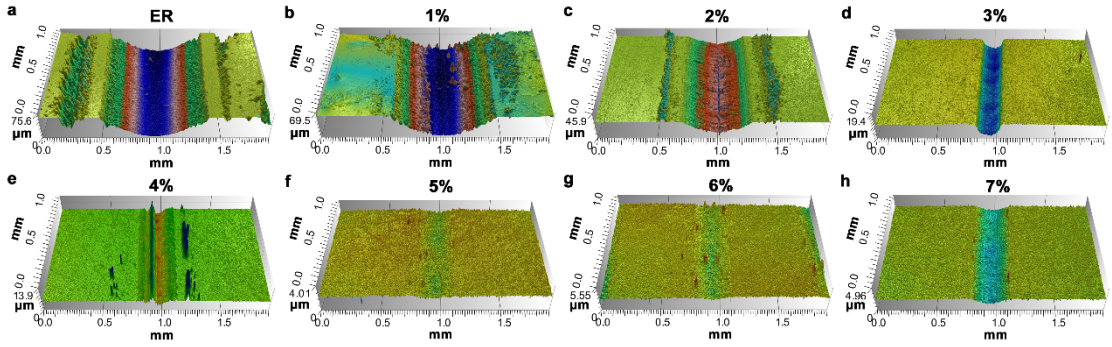

Figure 4 3D surface morphology and height of worn tracks at 10 N measured by Rtec UP-Lambda for (a) ER, (b) EC1, (c) EC2, (d) EC3, (e) EC4, (f) EC5, (g) EC6 and (h) EC7.

Figure 4 depicts the 3D surface morphology and height of worn tracks at 10 N measured by Rtec UP-Lambda for ER and ECs. After blending the graphene, the width and depth of ECs were smaller than those of pure ER. This indicates that the wear resistance of ECs is enhanced compared with that of pure ER. Width and height of wear track for pure ER is the greatest (Fig. 4(a)), and those of the EC5 are the smallest (Fig. 4(f)). By increasing the graphene content of the composite, the depth of wear tracks decreases firstly to the lowest at EC5, and then increases. Width and depth

of wear tracks for pure ER are 934 and 68 μm (Fig. 4(a)) respectively, while those of EC5 are 311 and 0.45 μm correspondingly. Width and depth of wear track for ER are 3 and 151 times those of the EC5, respectively, revealing the unprecedented enhancement of wear resistance of the latter are 628 times that of the former.

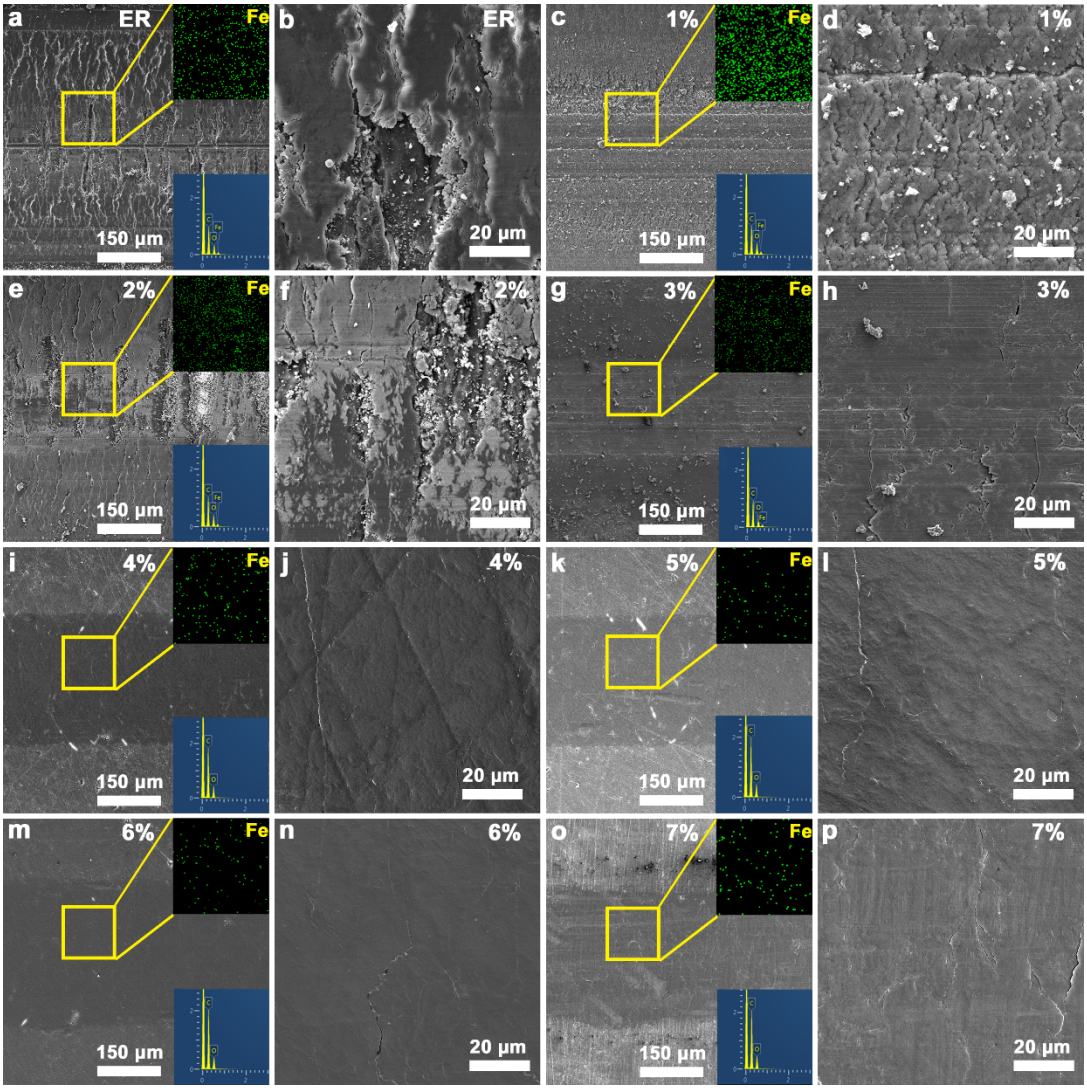

Figure 5 SEM images of worn tracks at 10 N for (a), (b) ER, (c), (d) EC1, (e), (f) EC2, (g), (h) EC3, (i), (j) EC4, (k), (l) EC5, (m), (n) EC6, and (o), (p) EC7 at low (a), (c), (e), (g), (i), (k), (m), (o) and their high (b), (d), (f), (h), (j), (l), (n), (p) magnifications marked by corresponding yellow squares. Insets in each figure showing the corresponding mapping of iron and EDS spectra taken from an area marked by a yellow square.

Figure 5 shows the scanning electron microscopy (SEM) images of worn tracks at 10 N for ER and ECs at low and high magnifications. Cracks are most severe on the wear track of pure ER (Figs.

5(a) and 5(b)), indicating the biggest wear rate (Fig. 3(b)) and worn volume (Fig. 4(a)). Cracks of ER after sliding in Figs. 5(a) and 5(b) are in good agreement with those of ER in previous reports.[23,24,43,51] This is attributed to the brittle nature of solidified ER and internal stress formed during curing.[2,15] A lot of cracks are found on worn tracks of EC1 (Figs. 5(c) and 5(d)) and EC2 (Figs. 5(e) and 5(f)), meaning the most severe wear extent in ECs. The wear extent for EC3 (Figs. 5(g) and 5(h)) is in the middle of ECs, and those of EC4 (Figs. 5(i) and 5(j)), EC5 (Figs. 5(k) and 5(l)), EC6 (Figs. 5(m) and 5(n)) and EC7 (Figs. 5(o) and 5(p)) are the lowest in Fig. 5. The sliding direction could be carefully identified along the horizontal one for EC3, EC6 and EC7 (Figs. 5(h), 5(n) and 5(p)). By increasing the content of graphene from 3 to 7 wt.%, the widths of the wear tracks are reduced (Figs. 5(g), 5(i), 5(k), 5(m) and 5(o)), in comparison with those of pure ER (Fig. 5(a)), EC1 (Fig. 5(c)) and EC2 (Fig. 5(e)). A small scratch on the pristine surface is left after sliding on the wear track of EC5 below the yellow square (Fig. 5(k)), revealing the smallest worn depth. Although there are small cracks that are found on the worn track of EC5 (Fig. 5(l)), the sliding direction could not be discerned, demonstrating the lowest wear in Fig. 5. Iron is found in the energy dispersive spectroscopy (EDS) of insets for pure ER (Fig. 5(a)), EC1 (Fig. 5(c)), EC2 (Fig. 5(e)) and EC3 (Fig. 5(g)), whereas it is not observed in the EDS spectra of insets for EC4 (Fig. 5(i)), EC5 (Fig. 5(k)), EC6 (Fig. 5(m)) and EC7 (Fig. 5(o)). This induces the high density of iron in the mapping of insets for Figs. 5(a), 5(c), 5(e) and 5(g), and the low density of those for Figs. 5(i), 5(k), 5(m) and 5(o). The lowest density of iron is in the mapping of insets for EC5 (Fig. 5(k)) and EC6 (Fig. 5(m)).

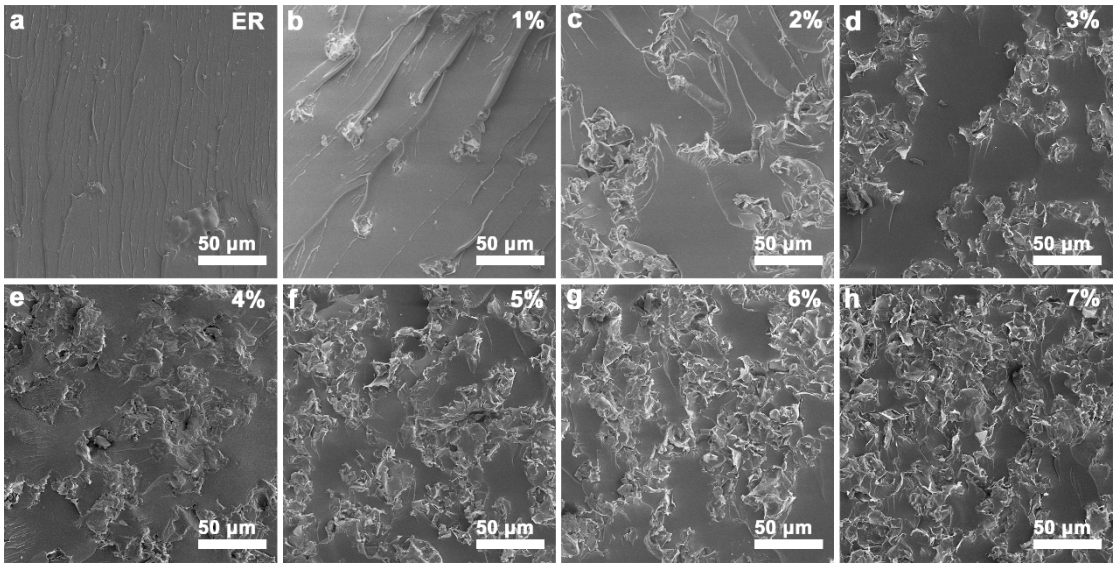

Figure 6 Cross-sectional SEM images of (a) ER, (b) EC1, (c) EC2, (d) EC3, (e) EC4, (f) EC5, (g)

EC6, and (h) EC7.

Figure 6 pictures the cross-sectional SEM images of ER and ECs. There are no graphene flakes in ER (Fig. 6(a)), and sporatic graphene flakes are found in EC1 (Fig. 6(b)). With increasing graphene to 2 wt.%, graphene flakes aggregate locally (Fig. 6(c)). For EC3, the aggregation phenomenon is improved partially (Fig. 6(d)). In EC5, graphene flakes distribute the most uniformly (Fig. 6(f)), corresponding to the lowest wear in Fig. 5(k). For EC4 (Fig. 6(e)), EC5 (Fig. 6(f)) and EC6 (Fig. 6(g)), graphene flakes distribute uniformly in ECs, resulting in the low wear in Figs. 5(i), 5(k), and 5(m), respectively. With increasing the content of graphene to 7 wt.%, graphene flakes accumulate locally, leading to the aggravation of wear (Fig. 6(h)).

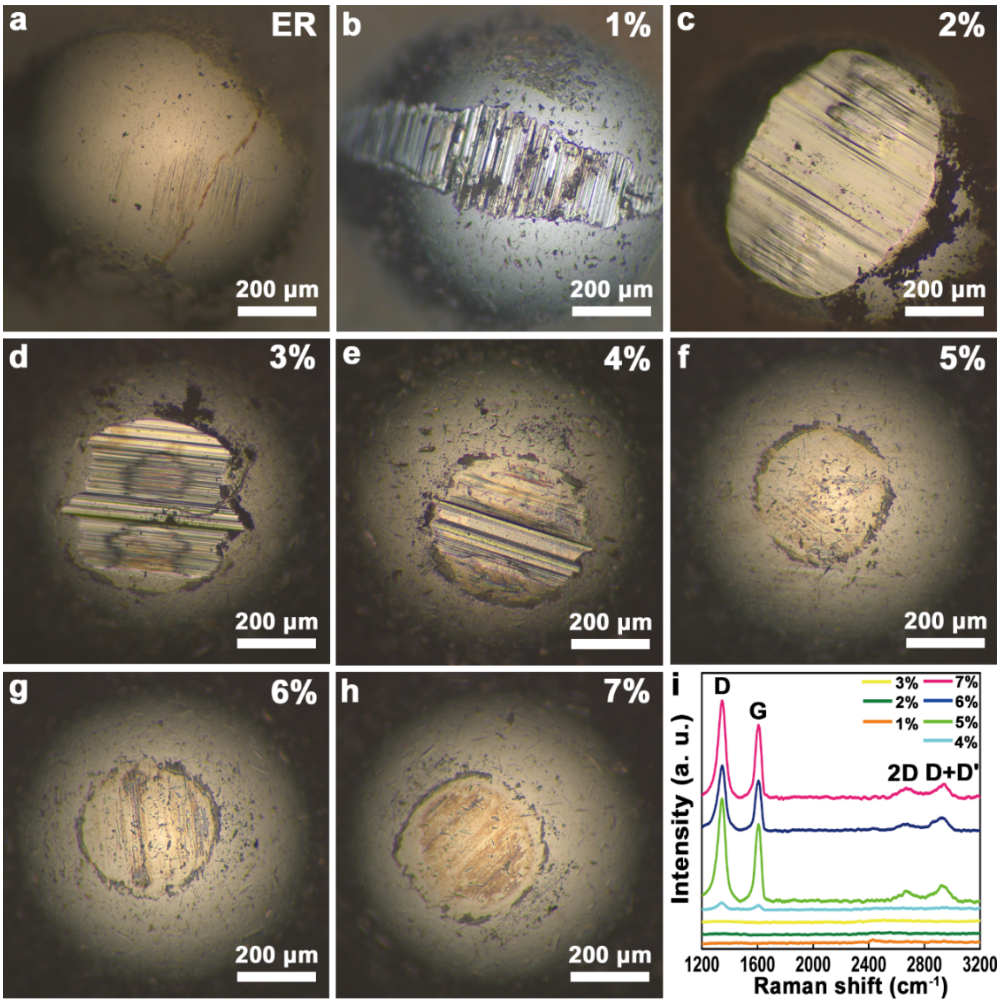

Figure 7 Optical images on worn surfaces of stainless-steel balls sliding with (a) ER, (b) EC1, (c) EC2, (d) EC3, (e) EC4, (f) EC5, (g) EC6, and (h) EC7, and (i) their Raman spectra.

Figure 7 illustrates the optical images on worn surfaces of stainless-steel balls sliding with ER, ECs and their Raman spectra. The contact area of the ball sliding with ER looks like an egg (Fig.

7(a)), while scratches on it are relatively small and the wear is less than those on surfaces of balls sliding with EC1, EC2, EC3 and EC4 (Figs. 7(b) to 7(e)). This was attributed to the brittle wear of ER. Hardness and Young's modulus of ER is 0.256 GPa[22] and 2.6 GPa[15] respectively, whereas those of 304 stainless steel are 1.863 GPa (190 HV, 1 GPa =102 HV) and 193 GPa, correspondingly.[55] In comparison, the hardness and Young's modulus of the stainless-steel balls are 7 and 74 times those of ER, respectively. As a tribopair, a stainless-steel ball is much harder than ER. Furthermore, melting points of 304 stainless steel and ER are 1454[58] and 390 °C[56] respectively, and thermal conductivities of them are 16.2[55,57] and 0.19[58,59] W $m^{-1}K^{-1}$, correspondingly. Due to the low thermal conductivity, melting point and fracture toughness of pure ER, the wear of the stainless-steel ball as a tribopair is less, even for the highest wear rate that happened on pure ER. However, when blending with graphene, mechanical properties and wear resistance of ER are intensified. This is because of the high specific surface area, two-dimensional (2D) planar geometry of graphene, and good adhesion between graphene and ER matrix induced by wrinkled rough surface of graphene.[24,41] Thus, the mechanical and tribological properties of ECs are efficiently reinforced.[46] As a result, the wear on surfaces of stainless-steel balls sliding with EC1, EC2 and EC3 is very severe (Figs. 7(b) to 7(d)). This is consistent with the presence of iron (Fe) element in mapping of insets of Figs. 5(c), 5(e) and 5(g). The worn width and length on surfaces of balls are 264 and 849 μm, 455 and 632 μm, and 473 and 481 μm sliding with EC1, EC2 and EC3, respectively. In addition, Raman spectra display that there is no graphene found on the worn surfaces of balls sliding with EC1, EC2 and EC3 (Fig. 7(i)). This indicates that there are no exfoliated graphene flakes during sliding between them. Graphene has an ultrahigh thermal conductivity of 3000[60-62] W $m^{-1}K^{-1}$, and extraordinary lubrication effect,[37-40] which is extremely significant to reduce the wear on surfaces of the balls.

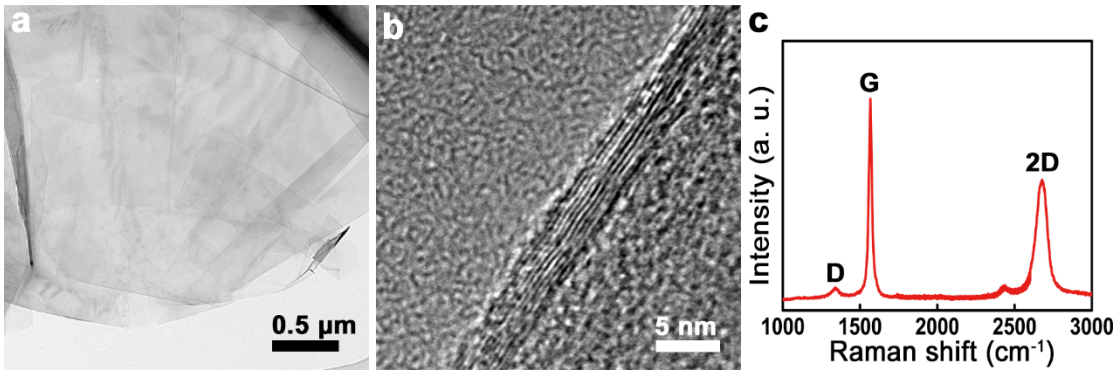

Figure 8 Front (a) and (b) cross-sectional views of TEM images and their Raman spectra (c) for

graphene prior to blending in ECs.

Graphene was found on the surface of the ball sliding with EC4 (Fig. 7(i)). With the presence of exfoliated graphene flakes, the wear of ball sliding with EC4 was alleviated, and the worn width and length were 376 and 392 μm, respectively. Peaks centered at 1350, 1580, 2700, and 2940 cm^{-1} are derived from D, G, 2D and D+D' peaks, respectively.[40] Figure 8 depicts the TEM images and their Raman spectra for graphene prior to blending in ECs. Ten-layer graphene is observed in Fig. 8(b). Prior to blending, the G peak is the highest, and 2D peak is much higher, and D peak is the lowest among three peaks, indicating the characteristics of single crystals (Fig. 8(c)).[39] In Fig. 7(i), D and G peaks on the surface of the ball sliding with EC4 were weak, indicating a small content of exfoliated graphene flakes in the debris. Consequently, the wear on the surface of ball with EC4 was obvious. Raman spectra on surfaces of the balls sliding with EC5, EC6 and EC7 (Figs. 7(f) to 7(h)) are stronger than those of balls with EC1, EC2, EC3 and EC4, resulting in less wear on the balls of the former than that of the latter. Raman spectra of the ball sliding with EC5 are the strongest, leading to the least wear on it. Among the three balls sliding with EC5, EC6 and EC7 respectively, Raman spectra of the ball with EC6 are the weakest, resulting in the highest wear among the three balls. Contact diameters of the three balls are 323, 335, and 350 μm sliding with EC5, EC6 and EC7 respectively. D+D' peak appears on the three balls with EC5, EC6 and EC7 (Fig. 7(i)), signifying increased graphene defects. It is a combination of phonons with various momenta activated by a defect.[40] In comparison with Fig. 8(c), for Raman spectra on three balls sliding with EC5, EC6 and EC7 (Fig. 7(i)), D peaks increase to the highest, 2D peaks decrease greatly, and D+D' peaks appear, revealing the increase of defects in graphene. This is consistent with the exfoliated graphene flakes during sliding, where they served as a lubricant. D peak needs a defect to activate, coming from the breathing modes of six-atom rings. G peak forms from the E_{2g} phonon at the center of Brillouin zone.[40] 2D peak was generated from the second order of D peak, taking place invariably without the need for activation. It was produced by a process, in which momentum conservation occurs for two phonons with inverse wave vectors.

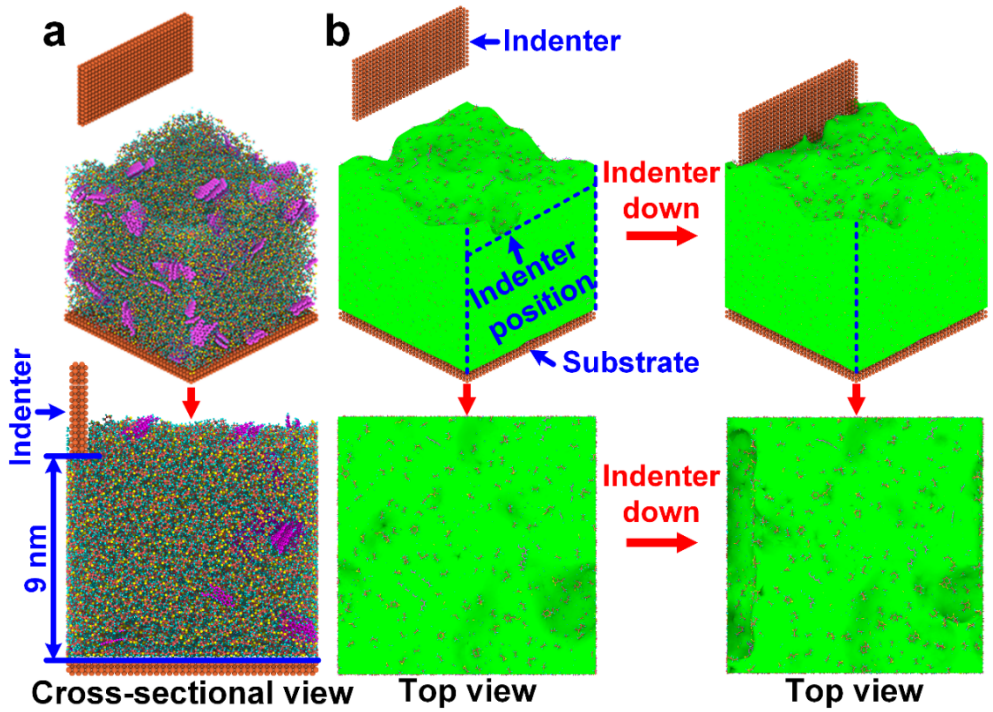

Figure 9 (a) Isometric and cross-sectional views, and (b) their schematic diagrams after curved surface treatment for MD model of EC10.73. Purple color showing the graphene flakes in (a).

To elucidate the enhancement mechanisms of graphene in ER, MD simulations on ECs were performed. In Figs. 2 and 3, the change of friction coefficient and wear rate is not drastic among EC5, EC6 and EC7, which takes difficulties to explore the enhancement mechanisms for ECs. In this regard, EC with 10.73 wt.% graphene (EC10.73) is employed to interpret the weakening mechanism of wear resistance in comparison with the EC with the highest wear resistance. Figure 8 depicts the isometric and cross-sectional views for MD models of EC10.73. An indenter-composite-substrate molecular structure is constructed in Fig. 9(a), which agrees well with those in previous reports.[46,49,51] The indenter is composed of Fe atoms in dimensions of 0.57×9.32×4.01 nm^3. It is square to increase the contact area, reducing the effect of indenting position on the influence of tribological properties. The Middle is EC, and the bottom is the substrate made of Fe atoms with sizes of 10.5×10.5×0.57 nm^3. Both the indenter and substrate were set as rigid bodies. Polymer consistent force field (PCFF)[63] was applied to ECs, describing the interactive forces in them. During MD simulations, periodical boundary conditions were exerted to x, y and z directions, and a vacuum layer was added to the z direction. EC was controlled by the Nose-Hoover thermostat in an NVT ensemble at 300 K for 500 ps, obtaining an equilibrated structure. After relaxation, ECs

were treated as curved surfaces (Fig. 9(b)), to simulate the actual ones in the experiments. During the sliding, the indenter was moved along the -z direction to the surface of ECs. When touching the surface, the indenter was moved downward at 0.008 Å/fs to a distance of 9 nm relative to the substrate, as indicated in the cross-sectional view shown in Fig. 9(a). When arriving at the position, the indenter was moved along the +x direction at 0.002 Å/fs, performing the sliding on the surfaces of ECs. During sliding, the lateral and normal forces were recorded, and then the friction coefficient was calculated.

Figure S6 shows force curves as a function of sliding distance, and their snapshots at different distances for EC with 7.14 wt.% graphene (EC7.14). Increasing the sliding distance enables the lateral and normal forces to stabilize and fluctuate along the average value, as shown in Fig. S6(a). Average values of forces for sliding distances from 2 to 8 nm were selected to calculate the friction coefficient. The friction coefficient calculated by MD simulations is 1.92 for EC7.14. In Fig. S6(b), more and more atoms accumulate ahead and aside the indenter, when increasing the sliding distance, and forming a groove behind the indenter.

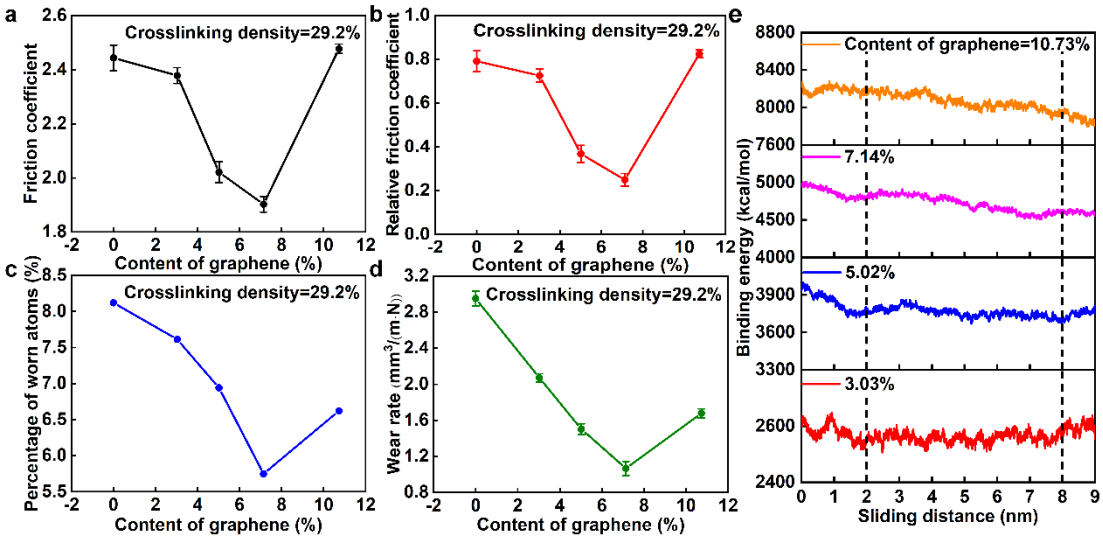

Figure 10 (a) Friction coefficient, (b) relative friction coefficient, (c) percentage of worn atoms, and (d) wear rate of ECs as a function of content of graphene, and (e) their binding energies as a function of sliding distance.

Figure 10 draws the friction coefficient, relative friction coefficient, percentage of worn atoms, and wear rate of ECs as a function of content of graphene, and their binding energies as a function of sliding distance. After blending the graphene flakes, all the friction coefficients of ECs are lower

than that of pure ER, except EC10.73 (Fig. 10(a)). Moreover, greater graphene flakes contents led initially to a lower friction coefficient, and then an increase, which is consistent with the experimental results shown in Fig. 2. The EC10.73 has the highest friction coefficient. Relative friction coefficient in Fig. 10(b) was obtained through subtracting 1.65 for each value in Fig. 10(a) respectively, making the lowest friction coefficient to be equal to that in experiments depicted in Fig. 2. The variation of relative friction coefficient in Fig. 10(b) is in good agreement with that in Fig. 2. The relative friction coefficient of ER is 0.79, which agrees well with the friction coefficient of ER in previous reports,[44] and is similar to that shown in Fig. 2. With blending graphene flakes, all the percentage of worn atoms and wear rate of ECs are lower than those of pure ER (Figs. 10(c) and 10(d)). Both the percentage of worn atoms and wear rate decrease firstly to the lowest value and subsequently increase, which is consistent with wear rates in experiments shown in Fig. 3. The EC7.14 occupies the lowest wear rate and percentage of worn atoms among four ECs (Figs. 10(c) and 10(d)). The interactive potential energy, E_{Inter} between ER and graphene is proposed,[49,51]

$$E_{Inter} = E_{Total} - E_{GF} - E_{ER} \qquad (3),$$

where, E_{Total} is the total potential energy of EC, E_{GF} is the potential energy of graphene flakes, and E_{ER} is the potential energy of ER. The binding energy, $E_{Bingding}$ is suggested between ER and graphene flakes,

$$E_{Binding} = -E_{Inter} \qquad (4).$$

Average binding energies of EC3.03, EC5.02, EC7.14 and EC10.73 are 2558, 3759, 4717, and 8065 kcal/mol, respectively at distances from 2 to 8 nm (Fig. 10(e)). Increasing the graphene content enabled more molecules to be absorbed on graphene flakes, resulting in an increase of binding energy.[48,51] Binding energy of ECs increases compared with that of pure ER, through blending the graphene flakes. This induces better stability of ECs than that of pure ER, resulting in the decrease of friction coefficient and wear rate.

For the EC3.03, friction coefficient decreases compared with that of pure ER as shown in Fig. 10(b). However, at low graphene content, there are no exfoliated graphene flakes adhering on the indenter during sliding, as depicted in Figs. 11(a) and 12(a), which is consistent with the Raman spectra in Fig. 7(i). Increasing the content of graphene to 5.02%, exfoliated graphene flakes during

sliding adhere on the indenter (Fig. 11(b)), which is in good agreement with the experimental results in Fig. 7(i). The adhered graphene flakes lubricate the indenter and EC, leading to the obvious decrease of friction coefficient in Fig. 10(b). When the content of graphene reaches to 7.14%, more exfoliated graphene flakes adhere on the indenter, and at its bottom there are graphene flakes, generating a better lubricating effect (Figs. 11(c), 12(b) and 13). This is consistent with the worn surface of the stainless-steel ball Fig. 7(f). With exfoliated graphene flakes at the bottom and on the surface of indenter, the friction coefficient of EC7.14 attains the lowest value among four ECs (Figs. 10(a) and 10(b)). In Fig. 10(e), the binding energies of EC5.02 and EC7.14 decrease rapidly at sliding distances from 0 to 2 nm, corresponding to the exfoliation of graphene flakes. However, when further increasing the content of graphene to 10.73%, graphene accumulates in the EC, as illustrated in Figs. 11(d) and 12(c), which is in good agreement with experimental results of Fig. 6(h). This increases the lateral force during sliding, resulting in the reduction of exfoliated graphene flakes on the surface and at bottom of the indenter (Figs. 11(d) and 12(c)), and increasing the friction coefficient and wear rate (Figs. 10(b) and 10(d)).

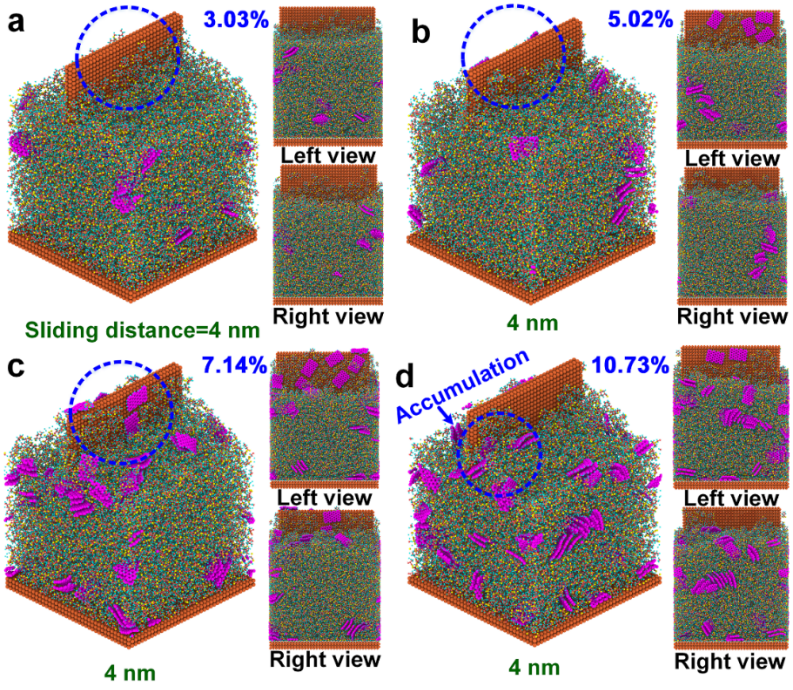

Figure 11 Snapshots of ECs with different contents of graphene at a sliding distance of 4 nm.

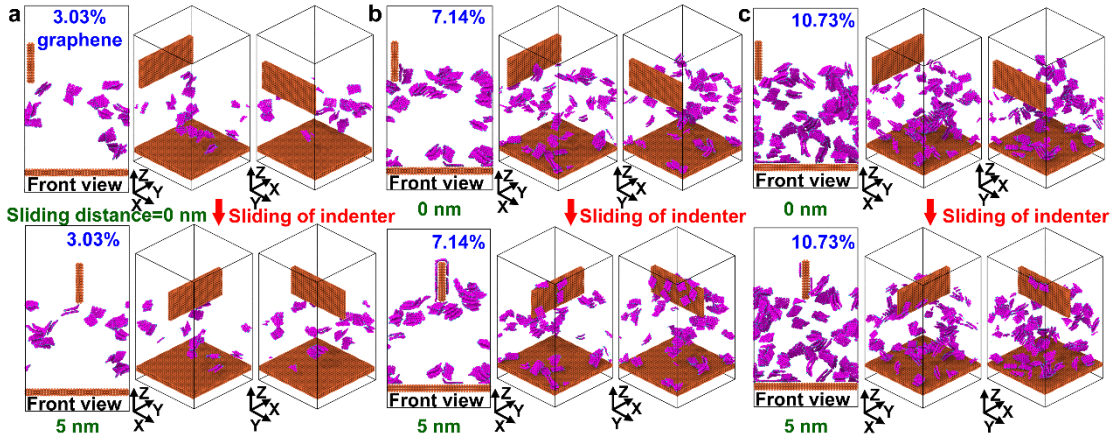

Figure 12 Snapshots of front and isometric views on distribution of graphene flakes by hiding the atoms of ER for (a) EC3.03, (b) EC7.14, and (c) EC10.73 at sliding distances of 0 and 5 nm, respectively.

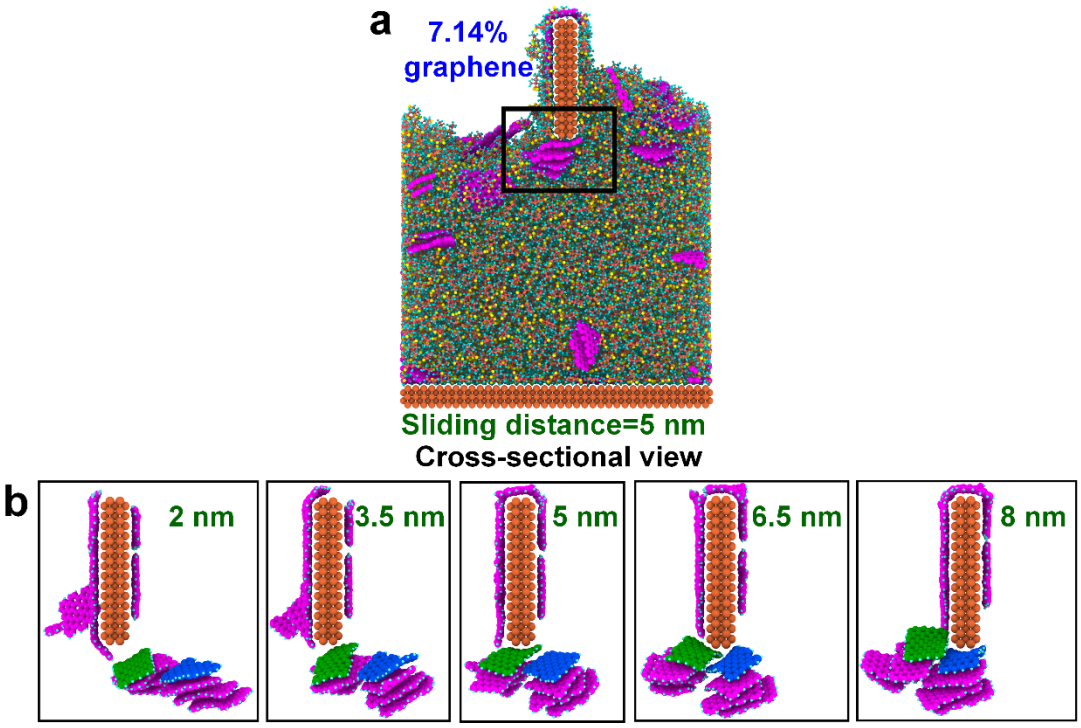

Figure 13 Cross-sectional views of snapshots for the EC7.14 at a sliding distance of (a) 5 nm and (b) snapshots by hiding the atoms of ER at different sliding distances. (b) showing the enlarged area marked by a black rectangle in (a) at different sliding distances. To identify the relative position between the indenter and graphene flakes clearly, graphene flakes are colored green, blue and purple in (b).

Figure 13 illustrates the cross-sectional views of snapshots for EC7.14 at different sliding distances. The EC7.14 has the lowest friction coefficient and wear rate among four simulated ECs.

During the sliding from 2 to 8 nm (Fig. 13(b)), graphene is always adhered on the front and back sides of the indenter. Especially for sliding distances of 5, 6.5 and 8 nm, graphene is adhered on the top side of the indenter. Graphene flakes are invariably at the bottom of the indenter during the sliding process, except at the beginning of 2 nm. This is different from those for the EC3.03 and EC10.73. For EC3.03, there is no adhered graphene on the indenter (Fig. 12(a)). Partial graphene is adhered on front and back sides of the indenter, and there is no graphene at the bottom of the indenter (Fig. 12(c)). The adhered graphene and graphene at the bottom of indenter contribute greatly to the lowest friction coefficient and wear rate.

Conclusions

In summary, seven kinds of ECs with different graphene contents were prepared. Wear resistance of EC5 was enhanced 628, 87, and 86 times greater than pure ER at 10, 8, and 6 N, respectively. Unprecedented wear resistance for the EC5 is greatly higher than the best reported 30-fold increase reported previously for ECs. At 10 N, friction coefficient and wear rates of ECs decrease first, and then increase with graphene loading. Raman spectra on the surface of the stainless-steel ball sliding with EC5 are the strongest, indicating the highest proportion of exfoliated graphene flakes. This results in the least wear on the surface of ball sliding with EC5. On the worn surfaces of three balls sliding with EC5, EC6 and EC7, D peaks increase to the highest, 2D peaks decrease greatly, and D+D' peaks appear, meaning an increase of defects of the graphene. This is consistent with exfoliated graphene flakes during sliding, where they served as a lubricant to enhance the wear resistance of ECs. The prepared ECs exhibit unprecedented wear resistance. These findings provide new insights to design and fabricate high performance devices based on developed ECs, for the use in coating, aerospace, and biomedical industries.

Experiments and simulations

$Nd(acac)_3$ (Aldrich Chemical Co., Inc., USA) was selected as a catalyst for cycloaliphatic ER solution (Dow Chemical Co., USA). $Nd(acac)_3$ was added in ER solution with a weight ratio of 1 to 1000, forming a binary solution. The binary solution was poured into a three-necked flask, and then the flask was put in an oil bath pan. The pan was heated to 80 ℃, and the binary solution was magnetically stirred at 80 ℃ for 8 h by a magnetic stirrer (DF-101s, Shanghai Lingke Industrial Development Co., Ltd., China). After magnetic stirring, the binary solution was cooled in air to

room temperature. MHHPA (Zhejiang Alpharm Chemical Technology Co., Ltd., China) was used as a curing agent. It was poured in the binary solution with a weight ratio of 95 to 100, producing a ternary solution. The ternary solution was stirred in a deaeration mixer (TM-310T, Shenzhen Smida Intelligent Equipment Co., Ltd, China) for 5 min to uniformly disperse the MHHPA into the ER. After uniform distribution of MHHPA in ER, eight specimens were prepared by blending graphene (Ningbo Morsh Technology Co., Ltd., China) in ER solution with 0, 1, 2, 3, 4, 5, 6, and 7 wt.%, respectively. To distribute the graphene in ER, the EC solution was stirred in the mixer for 5 min. After uniform mixing, the EC solution was decanted to a mold, and then the mold was placed in a vacuum oven (DZG-6050D, Shanghai Sumsung Laboratory Instrument Co., Ltd., China) to degas for 2 h at 45 ℃. After degassing, the EC solution was precured for 2 h at 135 ℃ in air. After precuring, the EC solution was solidified in air for 14 h at 165 ℃. Finally, the eight specimens were taken out from the oven and cooled to room temperature in air gradually.

Tribological experiments were performed on a tribometer (CETR-UMT-3, Bruker, USA) at room temperature with a relative humidity of 86%. Ball-on-disc reciprocating sliding tests were carried out on the tribometer. During testing, the normal load was set from 6 to 10 N, a stroke distance was 5 mm, the frequency was 2 Hz, and the sliding time was 30 min. Balls of 304 stainless steel with a diameter of 3 mm were employed as tribopair sliding with ER and ECs. Surface morphologies and volumes were measured by a noncontact optical profilometer (Rtec UP- Lambda, Rtec Universal Profilometer, California, USA). Worn tracks and their mapping and EDS spectra were characterized and measured by a FEI Sirion 200 FEG microscope. Worn surfaces on the stainless-steel balls as tribopair were measured and characterized by a confocal Raman microscope (inVia Reflex, Renishaw, UK), and a laser scanning confocal microscope (LSM 700, ZEISS, Germany).

MD models were constructed among epoxy monomers, MHHPA, and transition molecules. The epoxy monomer was 3-4 cyclohexyl methyl anhydride. The employment of transition molecules was in terms of alcoholysis reactions of the anhydride, leading to carboxylic acid groups to facilitate the construction of crosslinking models. The transition molecules were due to reactions between MHHPA and ethanol. Based on the experimental results, MD models were established with a weight ratio of 95 to 100 between MHHPA and ER. An MD model consisted of 1500 ER

monomers, 2100 MHHPA monomers and 30 transition molecules. It is an amorphous composite. ER and four EC models were constructed with 3.03, 5.02, 7.14, 10.73 wt.% graphene, respectively, with the atoms varying from 108360 to 117960. All the MD simulations were calculated by large-scale atomic/molecular massively parallel simulator (LAMMPS). The PCFF was applied to calculate intramolecular bonding and nonbonding reactions.[64,65] In MD simulations, a time step was set to 0.25 femtosecond (fs). After the construction, the models were treated by energy minimization using the conjugate gradient method. Then, the models were relaxed for 500 picoseconds (ps), in the NPT ensemble under 1 atmosphere pressure at 300 K along the x and y directions. Harmonic force was exerted to the z direction, stabilizing the length of the z direction of the models at approximately 100 Å. After relaxation, releasing the harmonic force in z direction, the models were further relaxed in NPT for 250 ps at 300 K under 1 atmosphere pressure along x and y directions. Finally, relaxation was completed, and non-crosslinked amorphous models with reasonable density were obtained. Periodic boundary conditions were applied to x, y and z directions, and a vacuum layer was added to the z direction.

Figure S7 depicts the molecular structure of an ER monomer, transition formula reacted between the curing agent and alcohol, and hydrogenated graphene. Equilibrated amorphous structure of EC needs to be performed by crosslinking, forming highly crosslinked 3D network. Crosslinking density, D_{cl} is expressed,

$$D_{cl} = \frac{N_{oER}}{N_{wER}} \qquad (5),$$

where N_{oER} and N_{wER} are the quantities of open loop and whole ER groups, respectively. Three reaction formulas during the curing process are proposed in Fig. S8,[51,63,66] consisting of reactions between ER and carboxylic acid (Fig. S8(a)), between ER and hydroxyl (Fig. S8(b)), and between hydroxyl in ER and anhydride (Fig. S8(c)). It is worthy to note that ER is a crosslinked polymer, while crosslinking in MD simulations is too time-consuming to be applied to a large model.[66] Hence, one,[51,63] three or eight[66] graphene sheets are usually incorporated in the polymer matrix, replacing that the graphene flakes distributed uniformly and randomly within the polymer. Additionally, the MD simulations are usually carried out by a commercial software, i.e. Materials Studio from Accelrys Inc. However, in this work, tribological mechanisms of graphene to ER was explored on

the surface of EC, and therefore graphene sheets incorporated in ER are not appropriate to compare to those published previously.[51,63,66] To be consistent with experiments, crosslinked MD models for ECs are necessary to be constructed, in which graphene flakes distribute in ER uniformly and randomly. To realize this objective, crosslinking of ER was conducted by the open source software of Polymatic through self-programming, and the flowchart is listed in Fig. S9. MD simulations were conducted by LAMMPS.

Crosslinking was performed in terms of the three reactions, listed in Fig. S8. The distance between reacted atoms plays an important role to conduct the crosslinking. For instance, if the distance between R1 and R2 is less than 10 Å, then R1 and R2 are connected (Fig. S8(a)). After the connection, the new bonds between R1 and R2 will be relaxed in the NPT ensemble (isothermal-isobaric system), at 300 K under 1 atmosphere pressure exerted to x and y directions for 100 ps. The modeling procedure is drawn in Fig. S9. The most important for crosslinking is to find an atomic pair between R1 and R2, between R1 and R3, and between R3 and R4 with a distance less than 10 Å. When the distance of atomic pairs is more than 10 Å, the temperature of model is increased under the NVT (canonical) ensemble at 600 K for 100 ps to increase the bonding probability. Operation limit for increasing temperature was set to 20 times to find the suitable atomic pairs for bonding. When reaching the limit, if there are no atomic pairs found, the crosslinking was terminated.[45,57] Crosslinking for ER consists of four steps. Firstly, prior to crosslinking, the hydrogen (H) atoms were removed from the carboxyl of the transition molecules after structure optimization, which was carried out by LAMMPS. Then, new bonds were constructed according to the distance between R1 and R2, R1 and R3, and R3 and R4, which was performed based on the three reactions shown in Fig. S8. To increase the speed of crosslinking, two criteria were employed. One is for increasing the temperature of the system, and the other is to extend the limit of distance for bonding, which was conducted by the collaboration between Polymatic and LAMMPS. Thirdly, chemical bonds between C and O atoms were cancelled for ER and anhydride in the curing agent, which was accomplished by self-programming. Finally, H atoms were added to the functional groups after the crosslinking, which was finished by self-programming.

Figure S10 illustrates the molecular structure of an MD model for ER with a crosslinking density of 29.2%. The MD model consists of 845 monomer molecules of ER, 408 monomer

molecules of the curing agent, and 30 transition molecules. The EC with an expected degree of crosslinking needs to be relaxed in the NPT ensemble, at 300 K for 250 ps at 1 atmosphere pressure to the x and y directions. Moreover, harmonic force was exerted to the z direction, controlling the length of the MD model in the z direction to approximately 100 Å. After relaxation, the harmonic force was removed. Then, the MD model was relaxed again for the NPT ensemble at 300 K and 1 atmosphere pressure to x and y directions for 250 ps, and finally the MD models of ECs with different contents of graphene were obtained.

Figure S11 shows the density of ECs as a function of graphene content. The density of pure ER is 1.155 g/cm^3, which is in good agreement with 1.142 g/cm^3 measured in experiments.[45] Increasing the content of graphene, the density of ECs increases monotonically to 1.19 g/cm^3, which is consistent with 1.186 g/cm^3 of crosslinked ER.[67]

Conflicts of interest

There are no conflicts of interest to declare.

Acknowledgments

The authors acknowledge the financial supports from the National Key R&D Program of China (2018YFA0703400), Changjiang Scholars Program of Chinese Ministry of Education, the Xinghai Science Funds for Distinguished Young Scholars and Thousand Youth Talents at Dalian University of Technology, and the Collaborative Innovation Center of Major Machine Manufacturing in Liaoning. Professor Parkin thanks the Chinese government for CSC scholarships and a visiting professorship, and EPSRC M3S CDT project (EP/L015862/1). Dr. Y. Lu acknowledges the Royal Society Research Grant (RGS\R1\201071).

Author Contributions

Z.Y.Z. and D.M.G. conceived the projects. Z.Y.Z. wrote the paper. Y.F.D. and L.C.G. designed and performed the tribological experiments. C.H.Z. and J.H.Z. conducted the molecular dynamics simulations. Y.L., J.H.Y. and I.P.P. analyzed the mechanism for increasing the wear resistance of ECs. All authors discussed the results and commented on the manuscript.

References

1 F. L. Jin, X. Li and S. J. Park, *J. Ind. Eng. Chem.*, 2015, **29**, 1-11.

2 N. Domun, H. Hadavinia, T. Zhang, T. Sainsbury, G. H. Liaghat and S. Vahid, *Nanoscale*, 2015,

7, 10294-10329

3 H. B. Gu, C. Ma, J. W. Gu, J. Guo, X. R. Yan, J. N. Huang, Q. Y. Zhang and Z. H. Guo, *J. Mater. Chem. C*, 2016, **4**, 5890-5906.

4 K. X. Shi, Y. C Shen, Y. W. Zhang and T. W. Wang, *Eng. Sci.*, 2019, **5**, 66-72.

5 P. F. Feng, L. C. Ma, G. S. Wu, X. R. Li, M. Zhao, L. L. Shi, M. Y. Wang, X. J. Wang and G. J. Song, *Compos. Sci. Technol.*, 2020, **200**, 108336.

6 L. L. Shi, G. J. Song, P. Y. Li, X. R. Li, D. Pan, Y. D. Huang, L. C. Ma and Z. H. Guo, *Compos. Sci. Technol.*, 2021, **201**, 108522.

7 J. Li, P. Zhang, H. He, S. P. Zhai, Y. Q. Xian, W. Ma and L. Y. Wang, *ES Energy Environ.*, 2019, **4**, 41-47.

8 X. H. Jing, J. Z. Wei, Y. X. Liu, B. Song and Y. Y. Liu, *Eng. Sci.*, 2020, **11**, 44-53.

9 H. J. Kang, Q. Shao, X. K. Guo, A. Galaska, Y. Y. Liu and Z. H. Guo, *Eng. Sci.*, 2018, **1**, 78-85.

10 D. G. Moore, L. Barbera, K. Masania and A. R. Studart, *Nat. Mater.*, 2020, **19**, 212-217.

11 D. Helmer and B. E. Rapp, *Nat. Mater.*, 2020, **19**, 131-133.

12 T. B. Sercombe and G. B. Schaffer, *Science*, 2003, **301**, 1225-1227.

13 J. R. Tumbleston, D. Shirvanyants, N. Ermoshkin, R. Janusziewicz, A. R. Johnson, D. Kelly, K. Chen, R. Pinschmidt, J. P. Rolland, A. Ermoshkin, E. T. Samulski and J. M. DeSimone, *Science*, 2015, **347**, 1349-1352.

14 Y. Shiraishi, T. Takii, T. Hagi, S. Mori, Y. Kofuji, Y. Kitagawa, S. Tanaka, S. Ichikawa and T. Hirai, *Nat. Mater.*, 2019, **18**, 985-993.

15 J. E. White, H. C. Silvis, M. S. Winkler, T. W. Glass and D. E. Kirkpatrick, *Adv. Mater.*, 2000, **12**, 1791-1800.

16 H. Watanabe and T. Kunitake, *Adv. Mater.*, 2007, **19**, 909-912.

17 L. J. Wang, C. Zhang, W. Gong, Y. B. Ji, S. H. Qin, L. He, *Adv. Mater.*, 2018, **30**, 1703992.

18 J. Bauer, A. Schroer, R. Schwaiger and O. Kraft, *Nat. Mater.*, 2016, **15**, 438-443.

19 O. Gutfleisch, K. Guth, T. G. Woodcock and L. Schultz, *Adv. Energy Mater.*, 2013, **3**, 151-155.

20 Y. Qian, S. Jiang, Y. Li, Z. Yi, J. Zhou, T. Q. Li, Y. Han, Y. S. Wang, J. Tian, N. Lin and Y. T. Qian, *Adv. Energy Mater.*, 2019, **9**, 1901676.

21 Y. Q. Zhu, C. Romain and C. K. Williams, *Nature*, 2016, **540**, 354-362.

22 A. Y. Adesina, I. H. Zainelabdeen, M. A. Dalhat, A. S. Mohammed, A. A. Sorour and F. A. Al-Badour, *Tribol. Int.*, 2020, **146**, 106244.

23 W. Brostow, W. Chonkaew, K. P. Menard and T. W. Scharf, *Mater. Sci. Eng. A*, 2009, **507**, 241-251.

24 X. J. Shen, X. Q. Pei, S. Y. Fu and K. Friedrich, *Polymer*, 2013, **54**, 1234-1242.

25 B. B. Chen, X. Li, Y. H., Jia, L., Xu, H. Y., Liang, X. F., Li, J., Yang, C. S., Li and F. Y. Yan, *Compos. Part A Appl. Sci. Manuf.*, 2018, **115**, 157-165.

26 Y. Zhang, Y. P. Yan, J. Guo, T. Y. Lu, J. Liu, J. Zhou and X. F. Xu, *ES Energy Environ.*, 2020, **8**, 42-47.

27 Y. L. Jia, P. W. Ren, J. Q. Wang, C. Z. Fan and E. J. Liang, *ES Energy Environ.*, 2020, **7**, 4-11.

28 N. Nidamanuri, Y. Q. Li, Q. Li and M. D. Dong, *Eng. Sci.*, 2020, 9, 3-16.

29 Y. Zhao, M. M. Niu, F. X. Yang, Y. Q. Jia and Y. H. Cheng, *Eng. Sci.*, 2019, **8**, 33-38.

30 N. Li, F. H. Zhang, H. Wang and S. F. Hou, *Eng. Sci.*, 2019, **7**, 72-79.

31 Y. Chen, Y. Wang, T. Su., J. Y. Chen, C. Zhang, X. X. Lai, D. W. Jiang, Z. J. Wu, C. Y. Sun, B. Li and Z. H. Guo, *ES Mater. Manuf.* 2019, **4**, 31-37.

32 C. Q. Liu, M. Chen, W. Yu and Y. He, *ES Energy Environ.*, 2018, **2**, 31-42.

33 Y. Gao, S. Kim, S. Zhou, H. C. Chiu, D. Nelias, C. Berger, W. de Heer, L. Polloni, R. Sordan, A. Bongiorno and E. Riedo, *Nat. Mater.*, 2015, **14**, 714-720.

34 E. M. Han, J. Yu, E. Annevelink, J. Son, D. A. Kang, K. Watanabe, T. Taniguchi, E. Ertekin, P. H. Y. Huang and A. M. van der Zande, *Nat. Mater.*, 2020, **19**, 305-309.

35 S. Kim, M. K. Gupta, K. Y. Lee, A. Sohn, T. Y. Kim, K. S. Shin, D. Kim, S. K. Kim, K. H. Lee, H. J. Shin, D. W. Kim and S. W. Kim, *Adv. Mater.*, 2014, **26**, 3918-3925.

36 S. Zhao, M. M. Niu, P. Peng, Y. H. Cheng and Y. Zhao, *Eng. Sci.*, 2020, **9**, 77-83.

37 S. Kawai, A. Benassi, E. Gnecco, H. Sode, R. Pawlak, X. L. Feng, K. Mullen, D. Passerone, C. A. Pignedoli, P. Ruffieux, R. Fasel and E. Meyer, *Science*, 2016, **351**, 957-961.

38 D. Berman, S. A. Deshmukh, S. K. R. S. Sankaranarayanan, A. Erdemir and A. V. Sumant, *Science*, 2015, **348**, 1118-1122.

39 Z. Y. Zhang, Y. F. Du, S. L. Huang, F. N. Meng, L. L. Chen, W. X. Xie, K. K. Chang, C. H.

Zhang, Y. Lu, C. T. Lin, S. Z. Li, I. P. Parkin and D. M. Guo, *Adv. Sci.*, 2020, **7**, 1903239.

40 O. Hod, E. Meyer, Q. S. Zheng and M. Urbakh, *Nature*, 2018, **563**, 485-492.

41 C. Chen, S. H. Qiu, M. J. Cui, S. L. Qin, G. P. Yan, H. C. Zhao, L. P. Wang and Q. J. Xue, *Carbon*, 2017, **114**, 356-366.

42 Y. W. Ye, D. W. Zhang, J. Y. Li, T. Liu, J. B. Pu, H. C. Zhao and L. P. Wang, *Corros. Sci.*, 2019, **147**, 9-21.

43 T. J. Bao, Z. Y. Wang, Y. Zhao, Y. Wang and X. S. Yi, RSC Adv., 2020, **10**, 26646-26657.

44 X. Li, B. B. Chen, Y. H. Jia, X. F. Li, J. Yang, C. S. Li and F. Y. Yan, *Surf. Coat. Technol.*, 2018, **344**, 154-162.

45 L. G. Zhang, G. Zhang, L. Chang, B. Wetzel, B. C. Jim and Q. H. Wang, *Tribol. Int.*, 2016, **104**, 225-236.

46 Y. L. Li, Q. Wang and S. J. Wang, *Compos Part B: Eng.*, 2019, **160**, 348-361.

47 R. Chawla, M. Dhawan and S. Sharma, *Proc. Inst. Mech. Eng. Part J J. Eng. Tribol.*, 2019, **233**, 1565-1573.

48 T. Onodera, J. Nunoshige, K. Kawasaki, K. Adachi, K. Kurihara and M. Kubo, *J. Phys. Chem. C*, 2017, **121**, 14589-14596.

49 Y. L. Li, S. J. Wang and Q. Wang, *Carbon*, 2017, **111**, 538-545.

50 Y. L. Li, S. J. Wang, Q. Wang and M. Xing, *Compos Part B: Eng.*, 2018, **133**, 35-41.

51 Y. L. Li, S. J. Wang and Q. Wang, *Compos Part B: Eng.*, 2017, **120**, 83-91.

52 W. C. Zhao, W. J. Zhao, Z. P. Huang, G. Liu and B. Wu, *Chem. Phys. Lett.*, 2019, **732**, 136646.

53 Y. X. Zhu, H. Y. Wang, L. Yan, R. Wang and Y. J. Zhu, *Wear*, 2016, **356-357**, 101-109.

54 J. F. Curry, T. F. Babuska, T. A. Furnish, P. Lu, D. P. Adams, A. B. Kustas, B. L. Nation, M. T. Dugger, M. Chandross, B. G. Clark, B. L. Boyce, C. A. Schuh and N. Argibay, *Adv. Mater.*, 2018, **30**, 1802026.

55 W. Q. Zhang, X. L. Wang, Y. J. Hu and S. Y. Wang, *Int. J. Mach. Tools Manuf.*, 2018, **130-131**, 36-48.

56 Y. F. Ai, L. Xia, F. Q. Pang, Y. L. Xu, H. B. Zhao and R. K. Jian, *Compos Part B: Eng.*, 2020, **193**, 108019.

57 Y. M. Zhang and W. B. Huang, *J. Manuf. Process.*, 2020, **57**, 324-333.

58 V. C. Doan, M. C. Vu, N. A. T. Thieu, M. A. Islam, P. J. Park and S. R. Kim, *Compos Part B: Eng.*, 2019, **165**, 772-778.

59 R. Wang, C. Z. Xie, S. K. Luo, H. S. Xu, B. Gou and L. L. Zeng, *Mater. Today Commun.*, 2020, **24**, 100985.

60 K. S. Novoselov, V. I. F. L. Colombo, P. R. Gellert, M. G. Schwab and K. Kim, *Nature*, 2012, **490**, 192-200.

61 S. Stankovich, D. A. Dikin, G. H. B. Dommett, K. M. Kohlhaas, E. J. Zimney, E. A. Stach, R. D. Piner, S. T. Nguyen and R. S. Ruoff, *Nature*, 2006, **442**, 282-286.

62 A. A. Balandin, *Nat. Mater.*, 2011, **10**, 569-581.

63 H. F. Zhan, G. Zhang, V. B. C. Tan, Y. Cheng, J. M. Bell, Y. W. Zhang and Y. T. Gu, *Adv. Funct. Mater.*, 2016, **26**, 5279-5283.

64 H. Heinz, R. A. Vaia, H. Koerner and B. L. Farmer, *Chem. Mater.*, 2008, **20**, 6444-6456.

65 K. Mirabbaszadeh and E. Zaminpayma, *Appl. Surf. Sci.*, 2012, **261**, 242-246.

66 S. C. Shiu and J. L. Tsai, *Compos Part B: Eng.*, 2014, **56**, 691-697.

67 H. Park and M. Cho, *J. Mech. Phys. Solids*, 2020, **142**, 103962.

Supplementary Information

Unprecedented enhancement of wear resistance for epoxy-resin graphene composites

Zhenyu Zhang,[1,†,*] Yuefeng Du,[1,†] Chunhua Zhu,[2,†] Liangchao Guo,[1] Yao Lu,[3] Jinhong Yu,[4] Ivan P. Parkin,[5] Junhua Zhao,[2,*] and Dongming Guo[1]

[1]*Key Laboratory for Precision and Non-Traditional Machining Technology of Ministry of Education, Dalian University of Technology, Dalian 116024, China.*

[2]*Institute of Mechanics and Advanced Materials, School of Mechanical Engineering, Jiangnan University, Wuxi 214122, China.*

[3]*Department of Chemistry, School of Biological and Chemical Sciences, Queen Mary University of London, London E1 4NS, UK.*

[4]*Key Laboratory of Marine Materials and Related Technologies, Ningbo Institute of Materials Technology and Engineering, Chinese Academy of Sciences, Ningbo 315201, China.*

[5]*Materials Chemistry Research Centre, Department of Chemistry, University College London, 20 Gordon Street, London, WC1H 0AJ, UK.*

†These authors contributed equally to this work. *e-mail: zzy@dlut.edu.cn; junhua.zhao@163.com

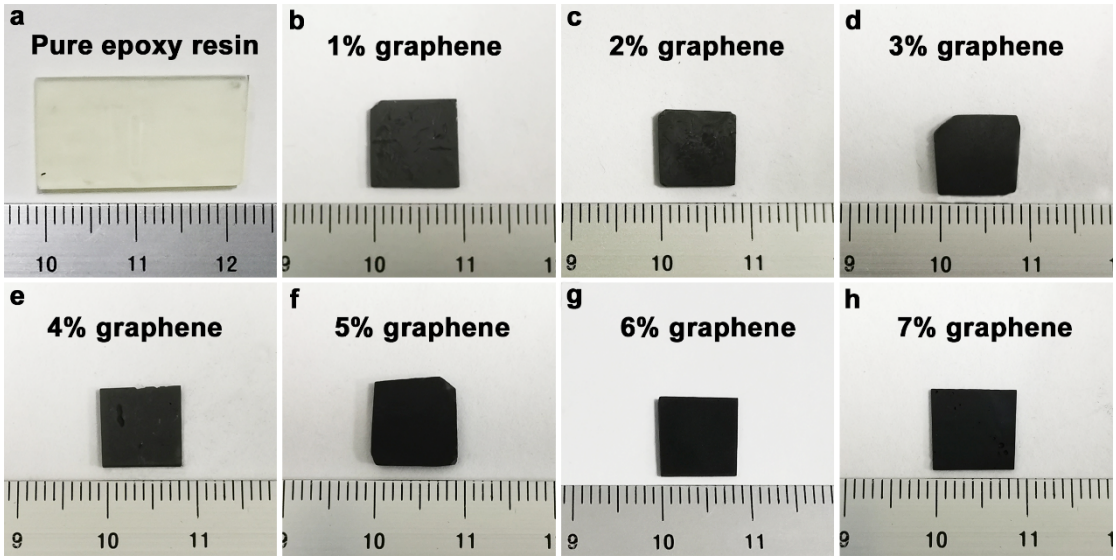

Figure S1 Photographs of prepared (a) pure ER, (b) EC1, (c) EC2, (d) EC3, (e) EC4, (f) EC5, (g) EC6, and (h) EC7.

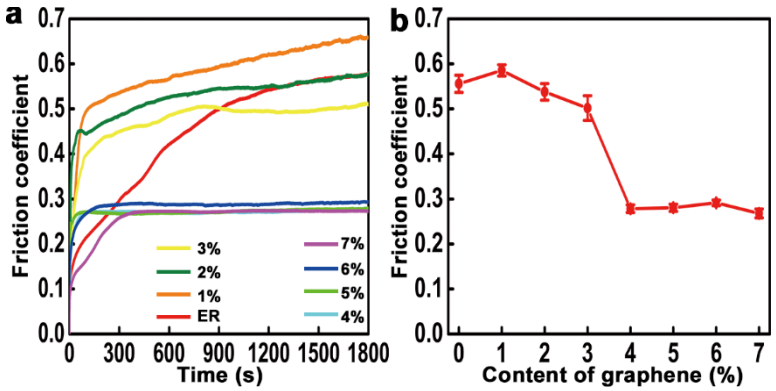

Figure S2 Friction coefficient of pure ER and ECs at 8 N as a function of (a) time and (b) content of graphene.

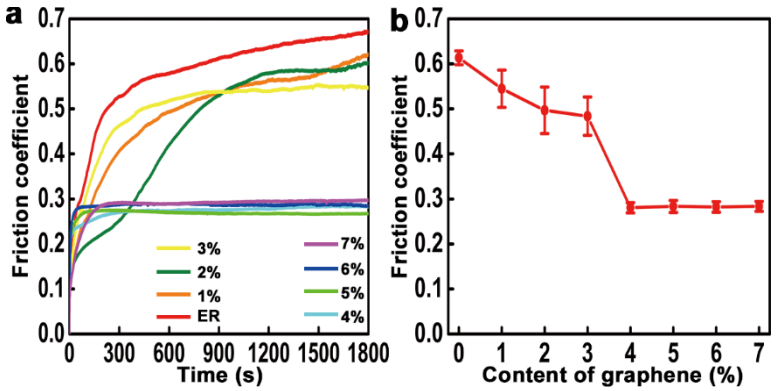

Figure S3 Friction coefficient of pure ER and ECs at 6 N as a function of (a) time and (b) content of graphene.

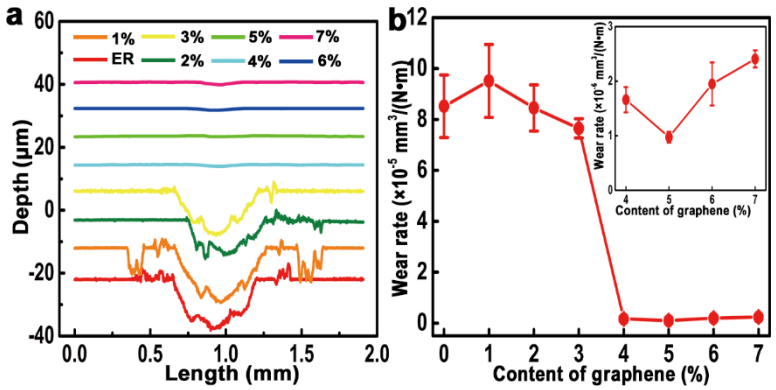

Figure S4 (a) Depth profile of wear tracks, and (b) wear rate at 8 N as a function of content of graphene for pure ER and ECs. Inset in (b) showing the corresponding enlarged part of wear rate as a function of content of graphene from 4 to 7 wt.%.

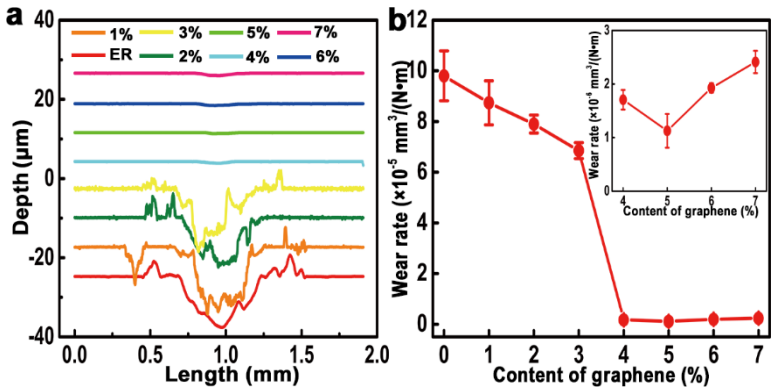

Figure S5 (a) Depth profile of wear tracks, and (b) wear rate at 6 N as a function of content of graphene for pure ER and ECs. Inset in (b) showing the corresponding enlarged part of wear rate as a function of content of graphene from 4 to 7 wt.%.

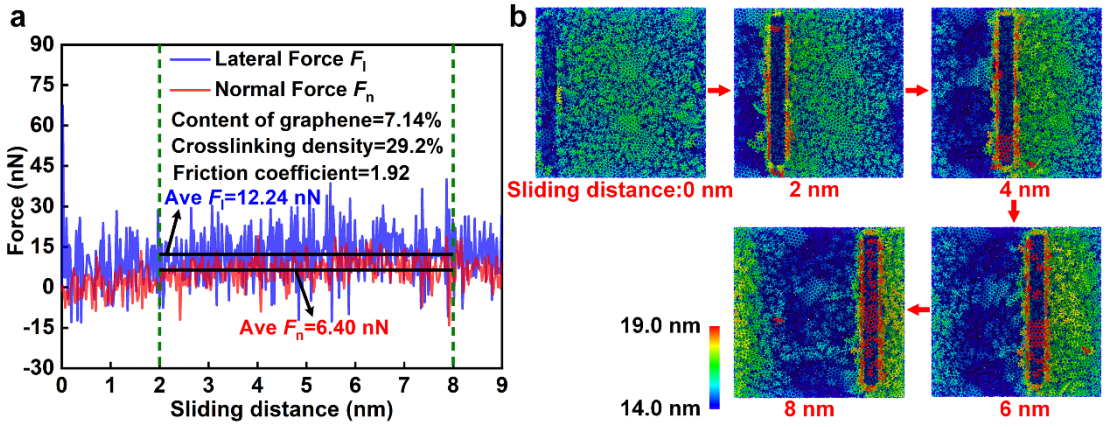

Figure S6 (a) Force curves as a function of sliding distance, and (b) their snapshots at different sliding distances for EC7.14. Atoms are colored according to their values of z coordinates.

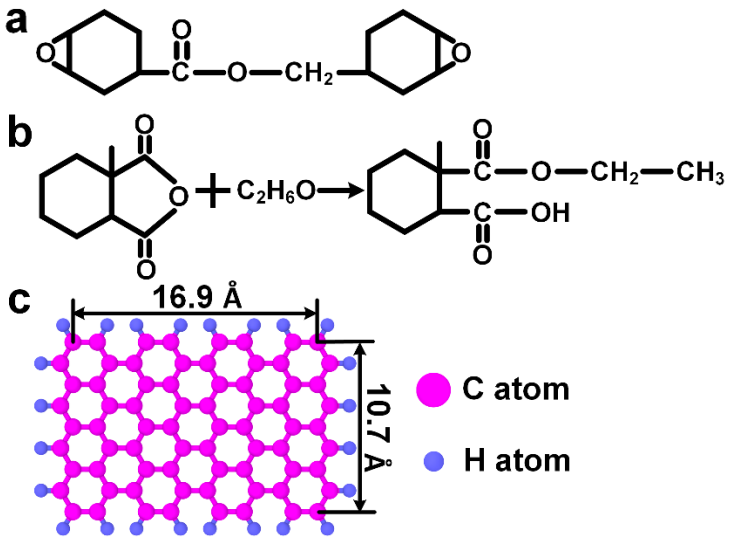

Figure S7 Molecular structure of (a) an ER monomer, (b) transition formula reacted between the

curing agent and alcohol, and (c) hydrogenated graphene by H atoms at the edges.

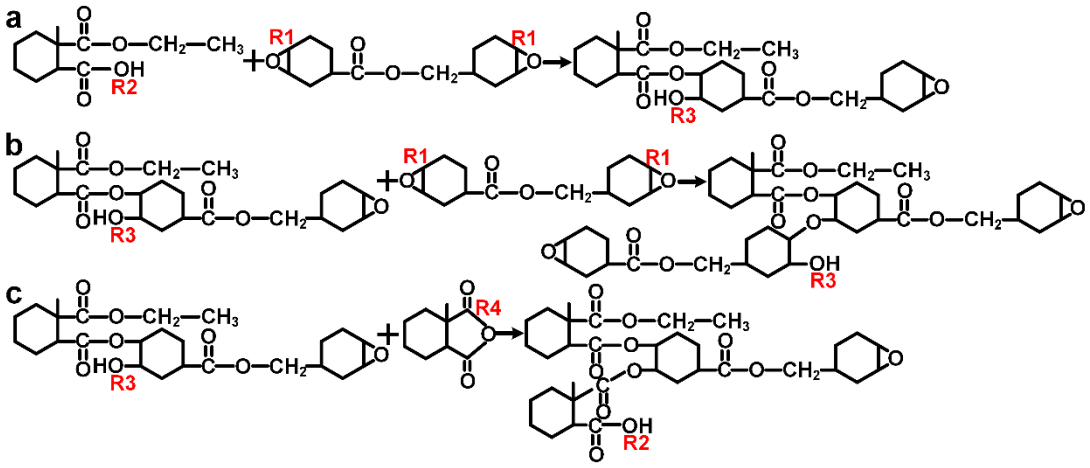

Figure S8 Reaction formulas between (a) ER and carboxylic acid, (b) between ER and hydroxyl, and (c) between hydroxyl in ER and anhydride during curing process. R1 denoting the C atoms in -CH_2- of ER, R2 standing for the oxygen (O) atoms in hydroxyl of transition molecules reacted between the curing agent and alcohol, and their resultant carboxyl groups, R3 meaning the O atoms in hydroxyl produced, and R4 representing the C atoms in anhydrate of monomer molecules in the curing agent.

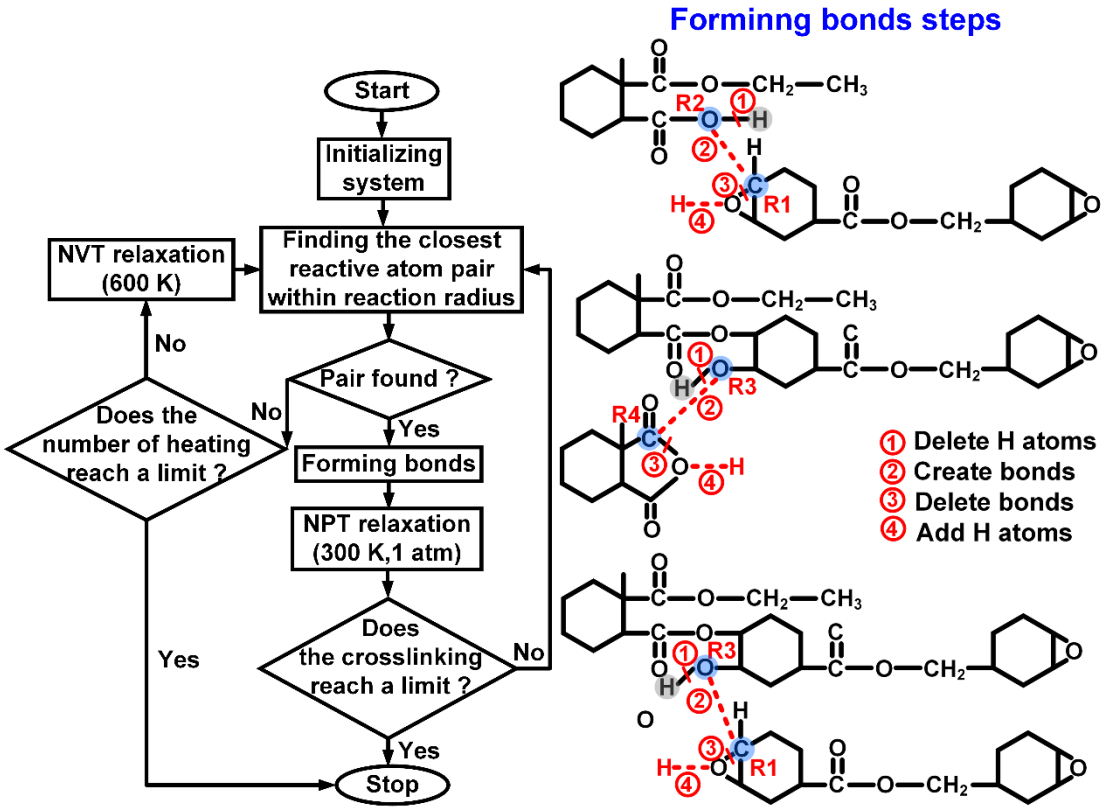

Figure S9 Flowchart of crosslinking for ER.

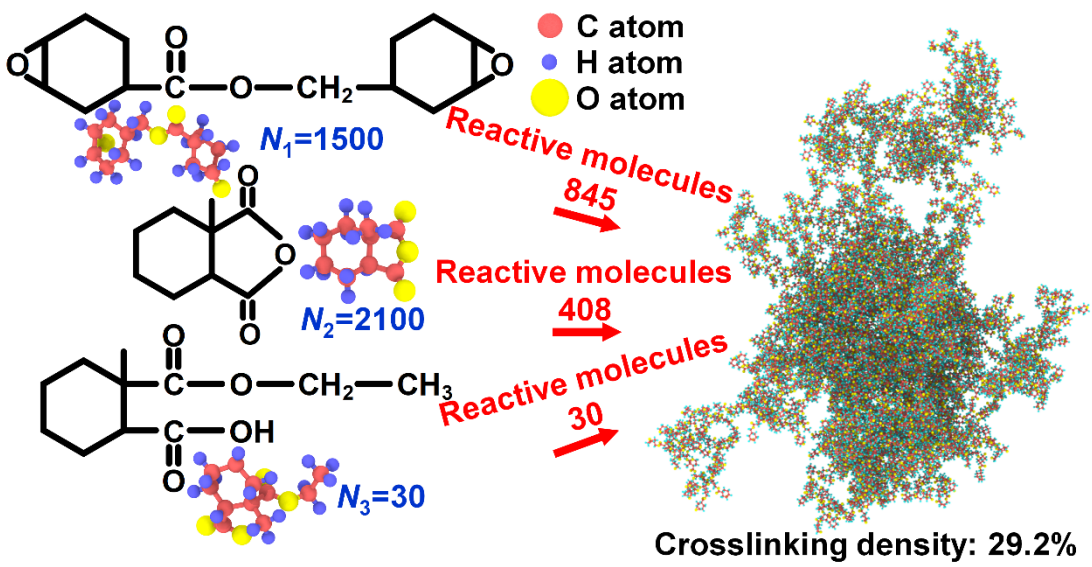

Figure S10 Molecular structure of an MD model for ER with a crosslinking density of 29.2%.

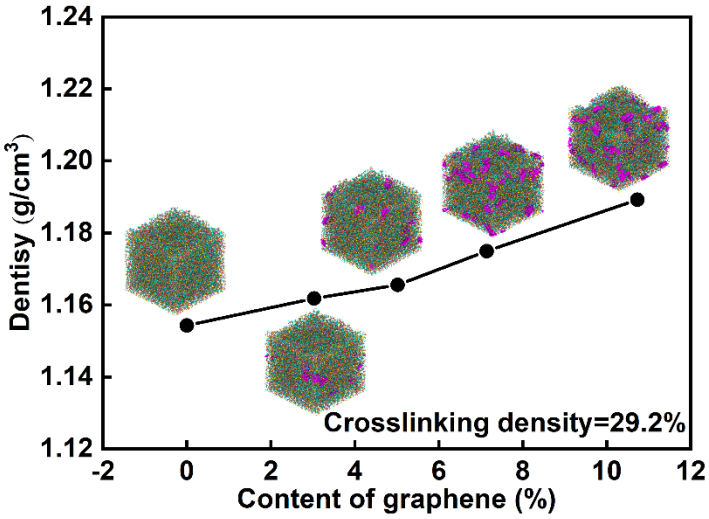

Figure S11 Density of ECs as a function of content of graphene. Purple color denoting the graphene flakes.